Comparison of Two Airfoils for Active Drag Reduction in Turbulent Flow

Marian Albers, Matthias Meinke, and Wolfgang Schröder

Abstract Active flow control of the turbulent flow over two airfoils of different shape is performed with the goal of increasing the overall aerodynamic efficiency. Large-eddy simulations are performed to investigate the impact of spanwise traveling transversal surface waves which are applied to a large percentage of the suction and the pressure side of the DRA2303 and NACA4412 airfoils at a chord based Reynolds number of $\mathrm{Re}_c = 400,000$. The results show a substantial decrease of the total integrated drag together with a slight increase of the lift. A detailed analysis reveals a decrease of the turbulent stresses and an attenuation of the boundary layer growth, resulting in an improvement of the lift-drag ratio for both airfoils.

Keywords Turbulent boundary layer · Drag reduction · Airfoil · Transversal traveling surface wave · Large-Eddy simulation · Active flow control

1 Introduction

Increasing energy efficiency in air travel is one of the keys to reduce global CO_2 emissions. Furthermore, even savings on the order of one percent in fuel consumption can be decisive in the competition between aircraft manufacturers and have a vast impact on airline economics. The drag of slender bodies moving in a fluid at high Reynolds numbers, e.g., aircraft in cruise flight, is to a large part determined by viscous friction, most often due to turbulent boundary layers developing around the wings and the fuselage. Therefore, reducing this friction drag has been of interest for the past decades. Drag reduction techniques can be classified by whether or not additional energy is introduced into the system. A further classification is possible by

---

M. Albers (✉) · M. Meinke · W. Schröder
Institute of Aerodynamics, RWTH Aachen University, W üllnerstrasse 5a, 52062 Aachen, Germany
e-mail: m.albers@aia.rwth-aachen.de

W. Schröder
JARA Center for Simulation and Data Science, RWTH Aachen University, Seffenter Weg 23, 52074 Aachen, Germany

W. E. Nagel et al. (eds.), *High Performance Computing in Science and Engineering '20*,
https://doi.org/10.1007/978-3-030-80602-6_18

considering techniques which delay or prevent transition from laminar to turbulent flow and techniques which alter the state of an already turbulent boundary layer, thereby reducing the viscous drag.

Among passive techniques, i.e., without the input of external energy, the best known approach is streamwise aligned surface protrusions, so-called riblets, which have proven to reduce friction drag in experimental [7] and numerical setups [12]. Moreover, they are one of the few technologies that have demonstrated to work on real aircraft in flight conditions [29]. Other passive techniques include compliant coatings [10] and superhydrophobic surfaces [15].

Active techniques, which require the introduction of external energy into the system, have the advantage of flexiblity of the control parameters, enabling an adjustment of the control to varying operating conditions. An extensive overview of active in-plane drag reduction techniques is given by [22]. Methods like spanwise oscillating walls [17] and streamwise traveling waves of spanwise wall velocity [23] are to be mentioned in this context. Furthermore, traveling transversal surface waves have shown promising results in experimental [19] and numerical studies [1, 4]. In general, these relatively new techniques have been investigated solely in canonical flow setups, e.g., Poisseuille flow and zero-pressure gradient turbulent boundary layer flow. Nevertheless, they are attractive due to the large potential drag reduction and the substantial attentuation of turbulent motion.

Most of the aforementioned methods, both passive and active, focus on reducing viscous drag in turbulent boundary layers. Many more techniques are available for bluff body flow control [9], i.e., control of the total drag of a body consisting of pressure and viscous drag. That is, a more global perspective needs to be taken into account, as the reduction of viscous drag might result in pressure penalties and vice versa [25]. The results of Reynolds-averaged Navier-Stokes simulations of a wing-body configuation in transonic flow with riblet surfaces [21] showed that not only, as is expected, the friction drag is lowered but that the passive technique influences the shock position and decreases also the pressure drag. Banchetti et al. [6] investigated drag reduction via streamwise traveling waves of spanwise wall velocity over a bump in a channel, i.e., a curved wall surface, and found an increase of the drag reduction for the curved geometry compared to the flat wall. A reduction of the skin friction on airfoils using, for instance, steady blowing can result in a thickening of the boundary layer, causing additional pressure drag from the wake, whereas the opposite can happen for steady suction [5]. Hence, a drag reduction technique is desirable which reduces friction drag while also preventing boundary layer growth, as has been shown for instance for body force control [26]. Another promising technique enabling such a favorable combination is spanwise traveling transversal surface waves for which a coupled decrease of pressure and viscous drag has been shown for airfoil flow [2]. We extend this study by considering another airfoil with a distinctively different geometry. A comparison between the effects of the drag reduction method on the flow over the two airfoils is presented to substantiate the applicability of the spanwise-traveling-wave approach to turbulent flow around slender bodies. Note that this contribution is based on the conference proceeding published in [3].

2 Numerical Method

The numerical method is a high resolution large-eddy simulation (LES) solving the filtered compressible unsteady Navier-Stokes equation on curvilinear grids. For the convective fluxes, the advection upstream splitting method (AUSM) is used, while a central scheme is employed for the viscous terms. The temporal integration is performed by an explicit 5-stage Runge-Kutta method of second-order accuracy. An implicit LES model is used, following the approach of monotonically integrated LES (MILES) by [8] such that the AUSM provides for the necessary dissipation for the smallest scales. Investigations by [20] have shown that no additional explicit turbulence model is required. The code has been used and verified for a wide range of flow problems, including turbulent boundary layer flow over moving surfaces [18] and turbulent airfoil flow [2].

3 Computational Setup

We compare the impact of a surface actuation technique on the flow field over two airfoils. The first geometry is a DRA2303 airfoil, designed for transonic flow [11], with a maximum thickness of 14% chord. The findings for this configuration are already discussed in detail in [2]. The second configuration is a NACA4412 airfoil, for which extensive DNS and LES studies exist [16, 28] and also drag reduction setups have been analyzed [5].

The flow around the airfoil is defined in a Cartesian domain defined by $\mathbf{x} = (x, y, z)$ and the corresponding flow velocities are denoted by $\mathbf{u} = (u, v, w)$. The chord of the airfoil is aligned with the x-axis and the spanwise coordinate is z. Periodicity in the spanwise direction is enforced to obtain an infinite span. The density is given by ρ and the pressure is denoted by p. The predictions are performed by solving the Navier-Stokes equations for unsteady compressible flow. The physical domain has an extent of 50 chords in the x- and y-direction and a width of 10% chord which is sufficient to resolve the largest turbulent scales [16]. A C-type curvilinear mesh is used to discretize the physical domain, the resolution in the wall-normal direction in the very near-wall region is $\Delta y^+|_{wall} < 1.6$ on the suction side and $\Delta y^+|_{wall} < 1.0$ on the pressure side with gradual coarsening off the wall. The resolution is $\Delta x^+ < 23.0$ in the wall-tangential direction and $\Delta z^+ < 9.0$ in the spanwise direction. An angle of attack of $\alpha = 5.0^\circ$ for the NACA airfoil and $\alpha = 2.0^\circ$ for the DRA airfoil is prescribed by adjusting the velocity vector of the incoming flow. A numerical tripping [24] at $x/c = 0.1$ on both sides of the airfoil triggers laminar-turbulent transition. The Reynolds number based on the chord length c is $\mathrm{Re}_c = u_\infty c/\nu = 400,000$ such that friction Reynolds numbers of up to $\mathrm{Re}_\tau = u_\tau \delta_{99}/\nu \approx 400$ are achieved. The Mach number is $\mathrm{M} = 0.1$.

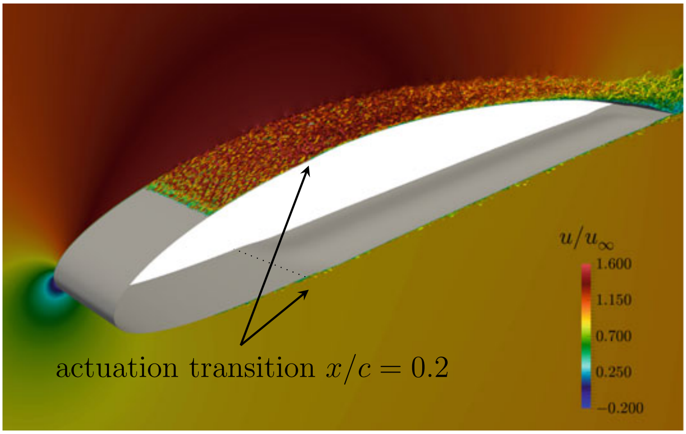

Fig. 1 Contours of the λ_2-criterion of the instantaneous velocity field of the actuated NACA4412 airfoil colored by the instantaneous streamwise velocity

A space- and time-dependent function

$$y_n^+|_{\text{wall}}(x, z^+, t^+) = A^+(x)\cos\left(\frac{2\pi}{\lambda^+}z^+ - \frac{2\pi}{T^+}t^+\right) \tag{1}$$

is applied to control the airfoil surface in the interval $x/c \in [0.2, 0.95]$ on the pressure and suction side such that a sinusoidal deflection of the solid wall in the wall-normal direction traveling in the spanwise direction is obtained. Smooth transitions from a non-actuated to an actuated wall and vice-versa are achieved via $1 - \cos(x)$ functions in the intervals $x/c \in [0.2, 0.25]$ and $x/c \in [0.9, 0.95]$. An illustration of the airfoil and the positions of the onset of the actuation is given in Fig. 1. The distributions of the parameters of the traveling wave function in inner scaling, i.e., the amplitude A^+, the wavelength λ^+, and the period T^+, non-dimensionalized by local values of u_τ, are shown in Fig. 2. A general difficulty in defining a reasonable distribution of the wave parameters is the strongly varying friction velocity along the airfoil chords, especially on the suction side of the NACA airfoil. Therefore, the parameters are chosen to lie in an interval whose bounds are relevant for the current airfoil flow. Based on the knowledge from previous studies the period is kept around a value of $T^+ \approx \mathcal{O}(50)$ (cf. Fig. 2b) and the wavelength is chosen as large as possible, i.e., one wavelength over the whole domain width. A near constant distribution of the amplitude in inner units (cf. Fig. 2c) for the NACA airfoil is achieved by a linear increase of the amplitude in outer scales (cf. Fig. 2d) along the chord on the suction side, on the pressure side a constant value is already adequate. In this regard, the NACA airfoil shows a favorable distribution of the skin-friction, being nearly constant on the pressure side and following a linear decrease on the suction side. In contrast, the distributions around the DRA airfoil create a more challenging situation such that a linear function for the increase of the amplitude in outer scaling does not result in a near-constant distribution in inner scales (cf. Fig. 2d).

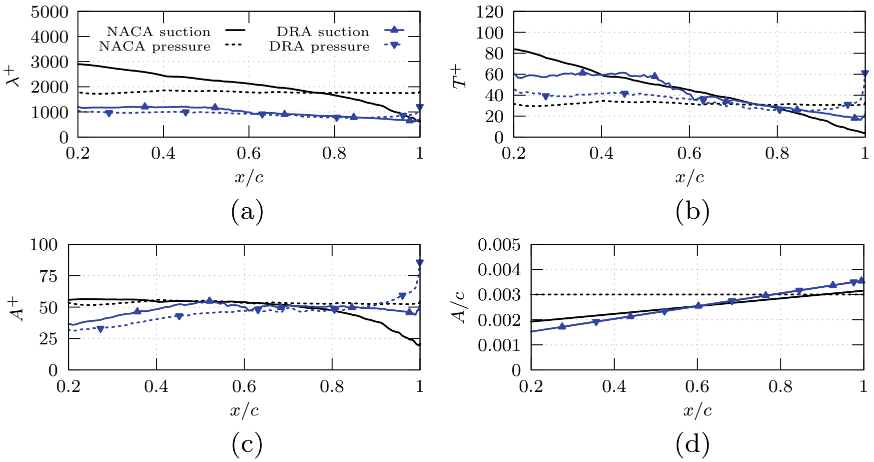

Fig. 2 Traveling transversal wave parameters **a** wavelength, **b** period, and **c** amplitude in inner scaling, and **d** amplitude in outer scaling

Details about the simulation procedure for the DRA airfoil can be found in [2], the simulations for the NACA airfoil are conducted as follows. First, the non-actuated reference setup is run for $tu_\infty/c \approx 24.0$ flow-over times until quasi-steady distributions of the lift and the drag are observed. Then, flow statistics were collected for $tu_\infty/c \approx 7$ flow-over times. Subsequently, the actuated setup is initialized with a converged flow field of the non-actuated reference case and the transition between solid wall and actuated wall is initiated. Once a quasi-steady state is observed statistics are gathered for the actuated flow.

4 Computing Resources

The accurate prediction of the flow field around airfoil wing sections with LES requires to resolve nearly the full spectrum of turbulent motions. That is, the mesh has a near-DNS resolution in the boundary layer and especially close to the wall. Therefore, even for moderate Reynolds numbers several hundred millions mesh points are required. Moreover, due to the small cells in the near-wall region and the explicit time-integration the time step is restricted by the CFL criterion to small values. However, the times until the airfoil flow reaches a stastical steady state are relatively long, since the developing wake flow has an important influence on the pressure distribution around the airfoil. The mesh for the NACA4412 simulation consists of $4698 \times 304 \times 301 \approx 4.3 \cdot 10^8$ points and a multi-block grid partitioning using balanced cut trees [14] is used to achieve a load-balanced distribution over all compute ranks.

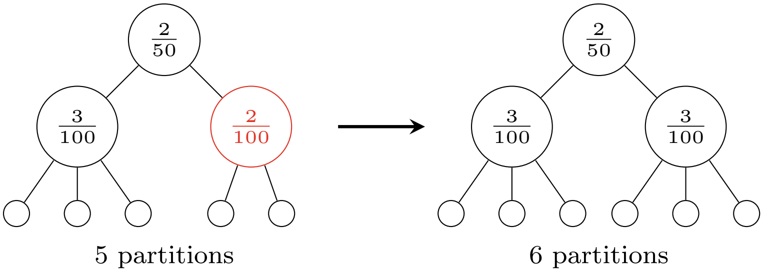

Fig. 3 Example of a balanced cut tree for a two-dimensional computational grid with $N_i \times N_j = 50 \times 100$ cells and (left) five partitions and (right) six partitions; the nodes are labeled with the ratio of children to the number of cells in that particular dimension; the node color red is chosen as an insertion point since the ratio of childs per cells is the lowest among all nodes

That is, for non-multi-block grids a single balanced cut tree is created with the number of tree levels equal to the number of grid dimensions plus one. For instance, as is also shown in Fig. 3, for a two-dimensional grid a cut tree with three levels is created. If only one partition is used the tree will contain only one node on each level. Each additional node on one of the levels below the top level represents a cut along the dimension associated with its level in the tree. The partitioning algorithm then traverses the tree to find an insertion point, i.e., the tree node with the highest ratio of the number of children to the number of cells in that particular dimension. If the selected node for insertion is no leaf node, all sub-trees of this particular node are reset. The sub-trees are filled recursively. The method guarantees that all partitions are themselves structured arrays, thus preserving the full optimization of the numerical code for structured grids. A detailed description of the method and an efficient extension for multi-block grids can be found in [14].

Partitioning of the hexahedral meshes results in n hexahedral sub-partitions, each of which is assigned to one rank. At the partition boundaries the flow variables are exchanged with neighbouring partitions with the message passing interface (MPI) in each Runge-Kutta substep. A strong scaling of the numerical code is shown in Fig. 4. It can be observed that a near optimum scaling is maintained up to 76, 800 cores, i.e., nearly half the available number of cores on Hazel Hen. The simulation of the NACA4412 cases were conducted using 200 compute nodes of the high-performance platform Hazelhen, where each node consists of two Intel® Xeon® E5-2680 v3 CPUs, i.e., a total of 4, 800 cores were used. The non-actuated simulations ran for 5m iterations until a quasi-steady state was observed, the actuated simulation was then restarted from the solution of the reference case and run for another 1.6 million iteration steps, which translates into about 8 flow over times. The simulation of the actuated case ran for about 368 h, i.e., about $1.7 \cdot 10^6$ core hours were used.

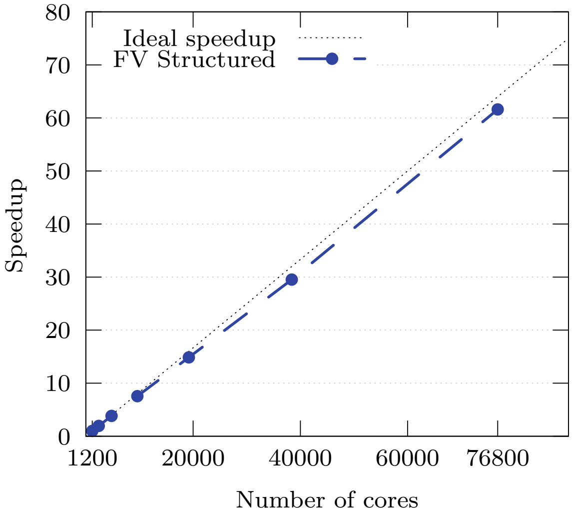

Fig. 4 Strong scaling of the numerical code on Hazel Hen

5 Results

Detailed results on the actuated flow around the DRA2303 airfoil are discussed in [2]. Therefore, statistics from this setup are shown primarily for a comparison with the new results on the NACA4412 airfoil, which we focus on in this study.

An illustration of the actuated flow field of the NACA4412 case is given in Fig. 1. However, no direct conclusion can be derived from the image since the majority of the flow modulation due to the control is confined to the near-wall region. Temporal distributions of the overall drag coefficient c_d, viscous drag coefficient $c_{d,v}$, and lift coefficient c_l for the NACA4412 airfoil are depicted in Fig. 5. Note that all distributions are normalized by the temporal average of the corresponding coefficient of the non-actuated reference case. Similar to the observations in [2], the viscous drag is directly affected after the initialization of the actuation and an averaged decrease of 12.9% is measured. For the DRA2303 case a decrease of 8.6% was achieved. The total drag (cf. Fig. 5b), i.e., the pressure contribution plus the viscous drag, shows the same tendency of being rapidly decreased. On average, it is 8.5% lower compared to the non-actuated reference case, which can be largely attributed to the decrease of the viscous part, whereas the pressure drag is modified by only 3.1%. The short time scale on which the modification of the integrated viscous drag takes place can be explained by the quick development of a periodically fluctuating secondary flow field with wall-normal and spanwise flow velocities above the traveling wave. This flow, resembling a directed oscillating Stokes layer with oscillating fluid instead of an oscillating plate, has an almost immediate effect, i.e., within few periods of the motion [27], on the turbulent structures, especially near the wall. A somewhat larger time scale is apparent for the modification of the lift (cf. Fig. 5c) which is mainly determined by the pressure distribution. Only after about $tu_\infty/c \approx 0.5 - 1.0$

Table 1 Overview of the change of the aerodynamic coefficients in percent of the two airfoils by the traveling wave actuation, negative values indicate an increase.

Case	Δc_d	$\Delta c_{d,v}$	$\Delta c_{d,p}$	Δc_l	$\Delta(L/D)$	ΔA_s
NACA	8.5	12.9	3.1	−1.4	−10.8	−0.5
DRA	7.5	8.6	5.0	−1.4	−9.6	−1.6

flow-over times a departure from the distribution of the non-actuated reference case becomes apparent and a new quasi-steady state is reached not before $tu_\infty/c \approx 4.0$ flow-over times after the onset of the actuation. A similar behavior was observed for the DRA2303 induced through the modified boundary layer and its decreased thickness, altering the flow over the trailing edge and in the wake region and thereby having a delayed effect on the overall pressure distribution. However, it is important to note that on average an increase of the lift by 1.4% is obtained. In combination with the lowered overall drag, this leads to an increase of the aerodynamic efficiency L/D by 10.8%. An overview of all alterations of the aerodynamic coefficients of both airfoils is given in Table 1.

The detailed changes of the skin-friction coefficient c_f are presented in Fig. 6 for the suction and the pressure side. On the suction side of both airfoils, the bulk of the skin-friction decrease is achieved in the forward part of the airfoil, i.e., $x/c < 0.5$, whereas further downstream the effect of the traveling wave actuation is steadily decreasing. This effect is a combination of a reduced efficiency of the control due to the increasing thickness-based Reynolds number of the boundary layer [13] and non-ideal control parameters. Especially the period T, which is constant in outer scaling, is in an efficient range only in a subdomain of the whole streamwise extent of the actuation. On the pressure side of the NACA airfoil, the skin-friction reduction shows a more constant distribution, with a considerable decrease even around $x/c \approx 0.9$. This advantageous behavior can be attributed to the much slower growth of the boundary layer, compared to the suction side, and a nearly constant skin-friction distribution in the reference case. Therefore, the values of the control parameters are in an effective interval over the whole extent of the actuated pressure side. In contrast, the skin-friction distribution on the pressure side of the DRA airfoil shows a decrease similar to the suction side, thus a reduced impact of the actuation can be expected.

A combined analysis of the skin-friction distribution (cf. Fig. 6) together with the momentum thickness distribution shown in Fig. 7 reveals an advantageous feature of this type of flow control. While the skin-friction distribution downstream of the end of the control region quickly recovers and approaches the non-actuated reference state, a persisting effect is evident in the momentum thickness. This was already observed in [26]. The decreased thickness of the actuated boundary layer holds till the trailing edge, resulting in the increased lift and the decreased pressure drag.

To obtain a high overall drag reduction, the streamwise extension of the control region is to be maximized otherwise a skin friction increase due to the decrease of the boundary layer thickness downstream of the control region, as described by

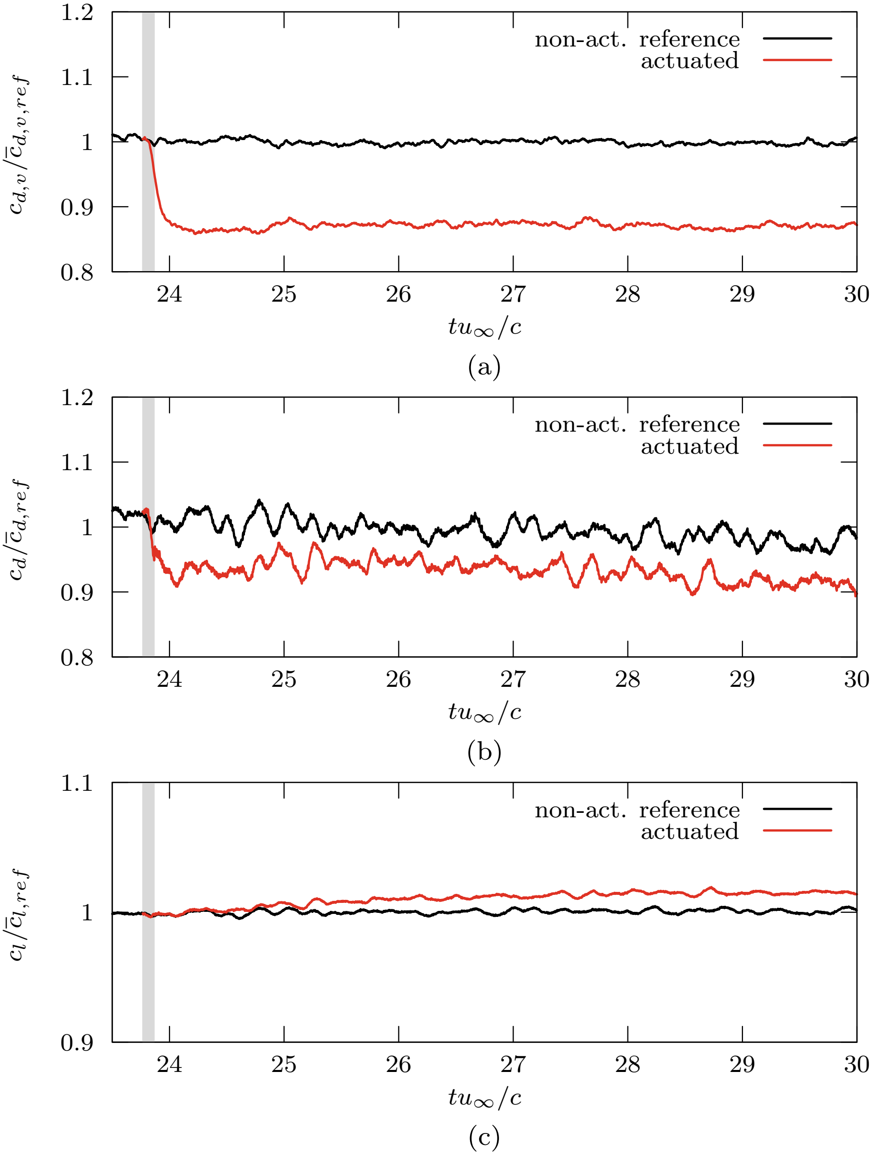

Fig. 5 Temporal distribution of **a** the viscous drag, **b** the total drag, and **c** the total lift of the NACA4412 airfoil of the non-actuated reference case and the actuated case, both normalized by the averaged coefficients of the non-actuated reference case

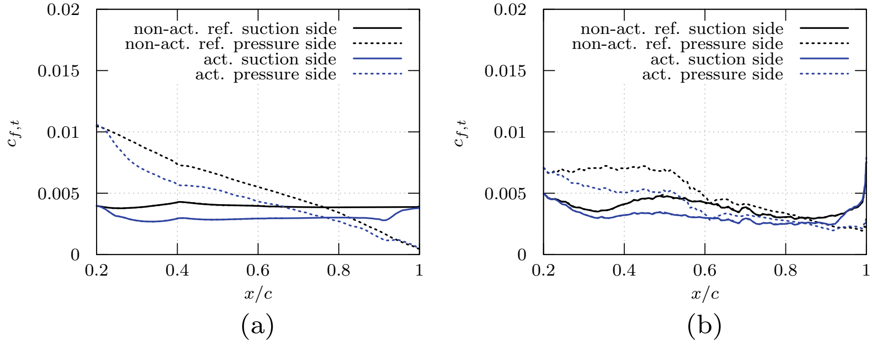

Fig. 6 Temporal and spanwise average of the wall-tangential skin-friction coefficient $c_{f,t}$ of **a** the NACA4412 cases and **b** the DRA2303 cases

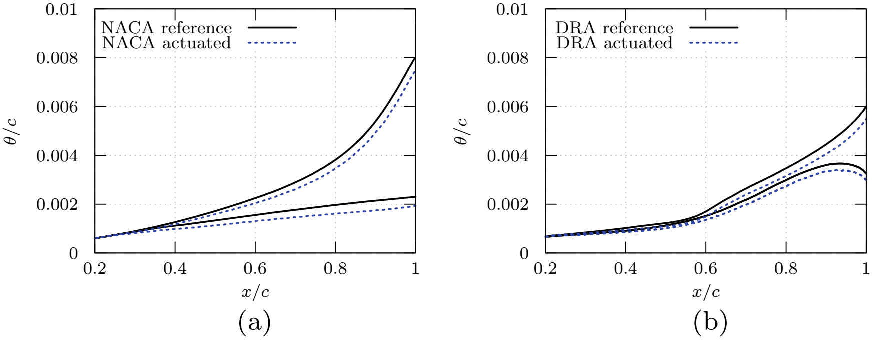

Fig. 7 Temporal and spanwise average of the momentum thickness θ on the suction (solid lines) and pressure side (dashed lines) of **a** the NACA4412 cases and **b** the DRA2303 cases

[26], deteriorates the global measured drag. Therefore, unlike for drag reduction investigations for canonical flows, such as turbulent channel flow or zero pressure gradient turbulent boundary layer flow, multiple additional factors contributing to the total aerodynamic efficiency have to be considered. A global perspective is necessary when evaluating the applicability of any drag reduction method to an airfoil [25]. A closer look at the second-order moments of the velocity and the vorticity is taken in the following. The turbulent velocity fluctuations across the boundary layer height for both airfoils are compared in Fig. 8 on the suction side at the chordwise position $x/c = 0.5$, which corresponds to a friction Reynolds number of $Re_\tau = 312$ for the NACA airfoil and $Re_\tau = 269$ for the DRA airfoil. Although the Reynolds number and the strength of the fluctuations is different at the same streamwise location, the effect of the control is similar. Reductions of all four components are apparent throughout the whole boundary layer. The reductions of the wall-tangential fluctutations are most pronounced. Due to the exceptionally strong attenuation in the near-wall region, i.e., $y^+ < 15$, a direct effect of the actuation on the near-wall streaks can be suspected, similar to spanwise oscillating wall [27]. Furthermore, the strong decrease of the

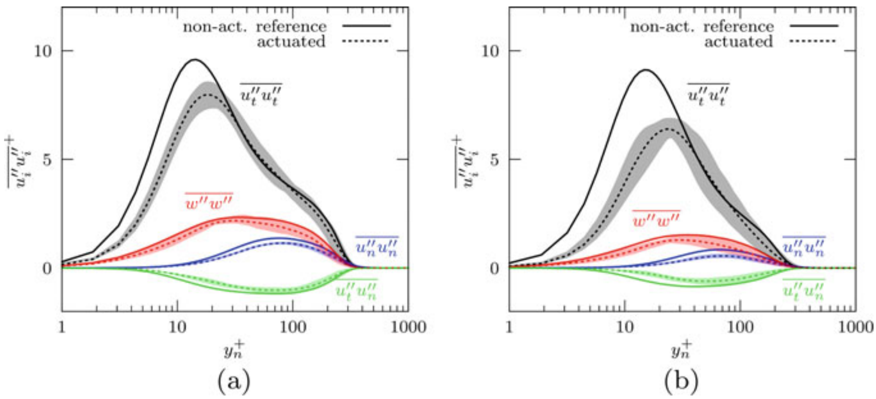

Fig. 8 Wall-normal distributions of the symmetric and the shear-stress components of the Reynolds stress tensor at $x/c = 0.5$ of **a** the NACA4412 cases and **b** the DRA2303 cases, normalized by the friction velocity of the non-actuated reference case. The shaded regions illustrate phasewise variations of the depicted quantity

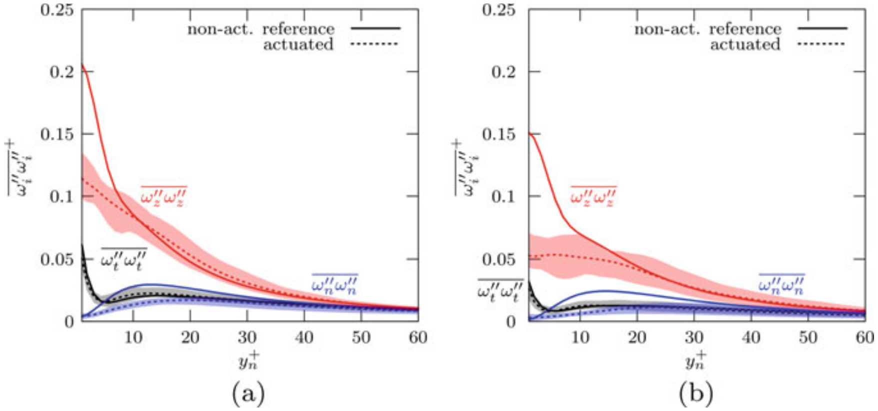

Fig. 9 Wall-normal distributions of the averaged vorticity fluctuations at $x/c = 0.5$ of **a** the NACA4412 cases and **b** the DRA2303 cases, normalized by the friction velocity of the non-actuated reference case. The shaded regions illustrate phasewise variations of the depicted quantity

shear stress, in relative terms, near the wall contributes strongly to the decrease of the skin friction.

This direct interference of the oscillating secondary flow field with the near-wall streaks, in opposition to quasi-streamwise vortices, is corroborated by the distributions of the averaged vorticity fluctuations depicted in Fig. 9. The wall-normal and spanwise vorticity fluctuations close to the wall, which are typically associated with near-wall streaks, are considerably damped. However, there is almost no variation of the wall-tangential component, which would evidence the existence of quasi-streamwise vortices.

6 Conclusion

Large-eddy simulations of turbulent airfoil flow for two airfoil shapes were conducted. The flow control method of spanwise traveling transversal surface waves was applied to the suction and the pressure side of a DRA2303 and of a NAC4412 wing section. The parameters of the time- and space-dependent actuation function were adjusted to be in an efficient range in inner scaling using the local skin-friction.

The results show a general decrease of the integrated viscous drag for both airfoils and also a slight reduction of the pressure drag. In combination with an increase of the lift, owing to a reduced boundary layer thickness at the trailing edge, the aerodynamic efficiency is improved for both airfoil shapes. Based on the current findings it can be stated that, the flow control technique – spanwise transversal surface waves – yields highly promising aerodynamic results for massively different airfoil shapes. Nevertheless, it has to be kept in mind that the airfoil shape and the developing boundary layers require to calibrate the control parameters of the actuation system, especially when a large percentage of the airfoil surface is subject to the control. Although the findings of this study are very promising with respect to active flow control and drag reduction, more details have to be investigated, e.g., higher Reynolds number flows, transonic flows with shocks, etc. are to be analyzed, to assess whether or not drag reduction can be achieved in cruise flight.

Acknowledgment Excerpts of this contribution have previously been published in the TSFP-11 conference proceedings [3]. The research was funded by the Deutsche Forschungsgemeinschaft (DFG) in the framework of the research projects SCHR 309/52 and SCHR 309/68. The authors gratefully acknowledge the Gauss Centre for Supercomputing e.V. (www.gauss-centre.eu) for funding this project by providing computing time on the GCS Supercomputers Hazel Hen at HLRS Stuttgart.

References

1. M. Albers, P.S. Meysonnat, D. Fernex, R. Semaan, B.R. Noack, W. Schröder, Drag reduction and energy saving by spanwise traveling transversal surface waves for flat plate flow. Flow Turb. Combust. **105**, 125–157 (2020). https://doi.org/10.1007/s10494-020-00110-8
2. M. Albers, P.S. Meysonnat, W. Schröder, Actively reduced airfoil drag by transversal surface waves. Flow Turbul. Combust. **102**(4), 865–886 (2019). https://doi.org/10.1007/s10494-018-9998-z
3. M. Albers, P.S. Meysonnat, W. Schröder, Influence of airfoil shape on active drag reduction efficiency. In: International Symposium on Turbulence & Shear Flow Phenomena (TSFP-11) (2019)
4. M. Albers, W. Schröder, Drag reduction for swept flat plate flow. Phys. Rev. Fluids **5**, 064611 (2020). https://doi.org/10.1103/PhysRevFluids.5.064611
5. M. Atzori, R. Vinuesa, G. Fahland, A. Stroh, D. Gatti, B. Frohnapfel, P. Schlatter, Aerodynamic effects of uniform blowing and suction on a NACA4412 airfoil. Flow Turb. Combust. **105**, 735–759 (2020). https://doi.org/10.1007/s10494-020-00135-z
6. J. Banchetti, P. Luchini, M. Quadrio, Turbulent drag reduction over curved walls. J. Fluid Mech. **896**, A10 (2020). https://doi.org/10.1017/jfm.2020.338

7. D.W. Bechert, M. Bruse, W. Hage, J.G.T.V.D. Hoeven, G. Hoppe, Experiments on drag-reducing surfaces and their optimization with an adjustable geometry. J. Fluid Mech. **338**, 59–87 (1997). https://doi.org/10.1017/S0022112096004673
8. J.P. Boris, F.F. Grinstein, E.S. Oran, R.L. Kolbe, New insights into large eddy simulation. Fluid Dyn. Res. **10**(4–6), 199–228 (1992). https://doi.org/10.1016/0169-5983(92)90023-P
9. H. Choi, W.P. Jeon, J. Kim, Control of flow over a bluff body. Ann. Rev. Fluid Mech. **40**(1), 113–139 (2008). https://doi.org/10.1146/annurev.fluid.39.050905.110149
10. K.S. Choi, X. Yang, B.R. Clayton, E.J. Glover, M. Atlar, B.N. Semenov, V.M. Kulik, Turbulent drag reduction using compliant surfaces. Proc. R. Soc. London Ser. A **453**(1965), 2229–2240 (1997). https://doi.org/10.1098/rspa.1997.0119
11. J.L. Fulker, M.J. Simmons, *An Experimental Investigation of Passive Shock/Boundary-Layer Control on an Aerofoil* (Vieweg+Teubner Verlag, Wiesbaden, 1997), pp. 379–400. https://doi.org/10.1007/978-3-322-90711-0_22
12. R. García-Mayoral, J. Jiménez, Drag reduction by riblets. Philos. Trans. R. Soc. London Ser. A **369**(1940), 1412–1427 (2011). https://doi.org/10.1098/rsta.2010.0359
13. D. Gatti, M. Quadrio, Reynolds-number dependence of turbulent skin-friction drag reduction induced by spanwise forcing. J. Fluid Mech. **802**, 553–582 (2016). https://doi.org/10.1017/jfm.2016.485
14. G. Geiser, W. Schröder, Structured multi-block grid partitioning using balanced cut trees. J. Parallel Distrib. Comput. **138**, 139–152 (2020). https://doi.org/10.1016/j.jpdc.2019.12.010
15. J.W. Gose, K. Golovin, M. Boban, J.M. Mabry, A. Tuteja, M. Perlin, S.L. Ceccio, Characterization of superhydrophobic surfaces for drag reduction in turbulent flow. J. Fluid Mech. **845**, 560–580 (2018). https://doi.org/10.1017/jfm.2018.210
16. S.M. Hosseini, R. Vinuesa, P. Schlatter, A. Hanifi, D.S. Henningson, Direct numerical simulation of the flow around a wing section at moderate Reynolds number. Int. J. Heat Fluid Flow **61**, 117–128 (2016). https://doi.org/10.1016/j.ijheatfluidflow.2016.02.001
17. W.J. Jung, N. Mangiavacchi, R. Akhavan, Suppression of turbulence in wall-bounded flows by high-frequency spanwise oscillations. Phys. Fluids A **4**(8), 1605–1607 (1992). https://doi.org/10.1063/1.858381
18. S. Klumpp, M. Meinke, W. Schröder, Drag reduction by spanwise transversal surface waves. J. Turbul. **11**, N11 (2010). https://doi.org/10.1080/14685248.2010.494606
19. W. Li, D. Roggenkamp, V. Paakkari, M. Klaas, J. Soria, W. Schröder, Analysis of a drag reduced flat plate turbulent boundary layer via uniform momentum zones. Aerosp. Sci. Technol. **96**, 105552 (2020). https://doi.org/10.1016/j.ast.2019.105552
20. M. Meinke, W. Schröder, E. Krause, T. Rister, A comparison of second- and sixth-order methods for large-eddy simulations. Comput. Fluids **31**(4), 695–718 (2002). https://doi.org/10.1016/S0045-7930(01)00073-1
21. B. Mele, R. Tognaccini, P. Catalano, Performance assessment of a transonic wing-body configuration with riblets installed. J. Aircraft **53**(1), 129–140 (2016). https://doi.org/10.2514/1.C033220
22. M. Quadrio, Drag reduction in turbulent boundary layers by in-plane wall motion. Philos. Trans. R. Soc. London Ser. A **369**(1940), 1428–1442 (2011). https://doi.org/10.1098/rsta.2010.0366
23. M. Quadrio, P. Ricco, C. Viotti, Streamwise-travelling waves of spanwise wall velocity for turbulent drag reduction. J. Fluid Mech. **627**, 161 (2009). https://doi.org/10.1017/S0022112009006077
24. P. Schlatter, R. Örlü, Turbulent boundary layers at moderate Reynolds numbers: inflow length and tripping effects. J. Fluid Mech. **710**, 5–34 (2012). https://doi.org/10.1017/jfm.2012.324
25. P.R. Spalart, J.D. McLean, Drag reduction: enticing turbulence, and then an industry. Philos. Trans. R. Soc. London Ser. A **369**(1940), 1556–1569 (2011). https://doi.org/10.1098/rsta.2010.0369
26. A. Stroh, Y. Hasegawa, P. Schlatter, B. Frohnapfel, Global effect of local skin friction drag reduction in spatially developing turbulent boundary layer. J. Fluid Mech. **805**, 303–321 (2016). https://doi.org/10.1017/jfm.2016.545

27. E. Touber, M.A. Leschziner, Near-wall streak modification by spanwise oscillatory wall motion and drag-reduction mechanisms. J. Fluid Mech. **693**, 150–200 (2012). https://doi.org/10.1017/jfm.2011.507
28. R. Vinuesa, P.S. Negi, M. Atzori, A. Hanifi, D.S. Henningson, P. Schlatter, Turbulent boundary layers around wing sections up to $Re_c = 1,000,000$. Int. J. Heat Fluid Flow **72**, 86–99 (2018). https://doi.org/10.1016/j.ijheatfluidflow.2018.04.017
29. M.J. Walsh, W.L. Sellers III., C.B. Mcginley, Riblet drag at flight conditions. J. Aircraft **26**(6), 570–575 (1989). https://doi.org/10.2514/6.1988-2554